Applicability of Experimentally Derived Local Droplet Distribution to the Fully Lagrangian Approach

Zuhaib Nissar *, Steven Begg, Guillaume de Sercey, Oyuna Rybdylova

Advanced Engineering Centre, School of Architecture, Technology and Engineering, University of Brighton, Brighton, BN2 4GJ, UK
*Corresponding author: z.nissar@brighton.ac.uk

Abstract

It is computationally challanging to simulate sprays by fully resolving the transport equations at the droplet scale [1]. Instead, recent work has identified that the fully Lagrangian approach (FLA) has the potential to reduce computational time in spray simulations [2, 3], while capturing complex processes in the flow such as droplet accumulation and droplet trajectory crossing [4]. In the FLA, the dispersed droplet phase is treated as a continuum [5]. All droplet parameters, including concentration, are calculated along the chosen trajectories by solving systems of ordinary differential equations . This approach to modelling sprays has the advantages of Lagrangian particle tracking and continuous formulations for the particle-gas flow. The method has been applied to the case of polydisperse evaporating sprays by extending the original FLA to account for droplet sizes; this method is known as the generalised FLA (gFLA). For the closure of the gFLA, local droplet size and velocity distributions at each location are required as the initial conditions. This information is used to obtain the new size distributions as the flow evolves. In previous work [2, 3], due to lack of experimental data, the initial distributions for droplet size were assumed to be log-normal and the same at all locations. Furthermore, it was assumed that the initial velocity is the same for all the droplets.

The present work focuses on the development of a new experimental approach to characterising sprays, which enables us to obtain local droplet size and velocity distributions at each location for all instances of time. A flat fan spray nozzle was chosen to continuously inject water under steady flow conditions at room temperature. The back-lit images of the spray were captured by a high speed camera at 84000 frames per second. A microscopic lens was attached to the camera which resulted in a field of view of 2.23 $\times$ 5.95 mm^2 and a resolution of 4.5 μm/pixel. The entire spray plume was captured by traversing the nozzle relative to the camera. In this way, a grid of multiple image batches were acquired. The structures in the atomised region were identified and tracked using an in-house image processing code. The statistical analysis of the data was used to obtain local droplet size and velocity distributions, which is required for the gFLA.

Keywords

Droplet distribution, atomisation, image analysis, optical diagnostics.

Introduction

Sprays have a wide range of applications in various industries, including healthcare and engineering, making the understanding of their formation and dynamics essential [1]. In healthcare, studying sprays is critical for determining the transmission of pathogens, and pulmonary drug delivery technologies rely heavily on sprays [6]. In surface coating applications, droplet distribution and deposition are factors that significantly influence product quality, and sprays are also used in humidification, which is crucial for air conditioning [7]. Therefore, it is essential to accurately predict droplet dynamics, size, and velocity distribution for making technologies based on sprays more efficient [8].

While there are well-developed simulation tools to model sprays [9, 10], existing methods are either computationally expensive or statistically unreliable, and it is extremely challenging to simulate sprays by fully resolving the transport equations to the droplet scale. Therefore, there is a need to develop new and more efficient simulation methods for practical applications, which involve more complex flows. One promising approach is the fully Lagrangian method (FLA) [5].

According to the FLA methodology, droplet phase fields such as concentration, size and velocity, are calculated along the chosen trajectories by solving systems of ordinary differential equations. This approach to modelling sprays has advantages of Lagrangian particle tracking and continuous formulations for the particle-gas flow. The method has been applied for the cases of polydisperse evaporating sprays by reformulating the FLA to account for droplet sizes. This method is known as the generalised FLA (gFLA) [3]. It has been demonstrated that the FLA has the potential to reduce computational time in spray simulations while capturing complex structures in the flow related to droplet accumulation and droplet trajectory crossing [2, 11].

However, in order to close the gFLA, local droplet size and velocity distributions are required as initial conditions at each location. This information is then used to obtain new size distributions as the flow evolves. In [3, 11], due to the lack of experimental data, it was assumed that the initial distributions for droplet size were log-normal and the same at all locations. Furthermore, it was assumed that the initial velocity is the same for all droplets. The practical application of the gFLA, therefore, necessitates a new experimental approach to characterizing sprays, which would provide droplet size and velocity distributions at each location. Current methods for obtaining this information are limited. For instance, point-wise measurement techniques [12] such as Phase Doppler Anemometry (PDA) only consider particles within narrow tolerance limits of sphericity. Corrugated ligaments and non-spherical particles are neglected in this process, resulting in an inaccurate representation of the particle size and velocity distributions. Additionally, a large grid of points must be considered to cover the entire region of interest in the spray, which can be time-consuming.

To address these challenges, a new experimental approach is needed to characterize sprays more accurately and provide droplet size and velocity distributions at each location. The paper is structured as follows. The development of the steady flow spray rig is discussed in Section 2. Some insights about the mechanisms leading to droplet breakup are discussed in Section 3. The image processing algorithm and methodology developed to obtain droplet size and velocity distributions are described in Section 4. The outcomes of this study are discussed in detail in Section 5.

Experimental setup

Spray flow spray rig

A Bosch pressure washer pump was used to draw deionized water from the reservoir into the common rail. The resulting flow was then directed to the flat fan nozzle through the outlet on the common rail. The experiments were performed under steady state conditions. The mass flow rate of water was measured using a Bronkhorst Coriolis mass flow meter. To ensure a steady flow, the mass flow rates were controlled using a PID controller. The schematic of the experimental rig is shown in Figure 1

Flat fan nozzle

In this study, a flat fan nozzle (BETE – BJH 0.28) was used in the experiments. This nozzle is manufactured by drilling the entry passage using a round-nosed tool, while the exit passage is milled using a V-shaped cutter with a very small angle. This creates an elliptical orifice at the intersection of the two passages [13]. Figure 2 shows the microscopic view of a flat fan nozzle. The nozzle features a $50°$ slit angle and an elliptical orifice with an equivalent diameter of 0.28 mm, specifically designed to produce a diverging liquid sheet. Figure 1 illustrates a microscopic image of the nozzle. The flow rate of the nozzle 5 kg/hour. As the discharge of the nozzle is directly proportional to the square root of the flow pressure, flow number (k; 0.043 as per manufacturers specifications) which is defined by $k = flow\ rate(l/min)/\sqrt{flow\ pressure\ (bar)}$, is used to calculate the injection pressure [13]. The calculated injection parameters of the nozzle are shown in Table 1.

Optical setup

The setup consists of a Phantom 5150 camera attached with a K2 Infinity long-distance microscopic lens, which provided high magnification and resolution. The field of view of the setup captures an area of 5.95×2.23 mm^2 or 480×1280 pixels^2, with a resolution of 4.6 μm per pixel. The depth of field was less than 3mm. The frame acquisition rate was set to 84000 frames per second. The setup captured

Table 1. Injection parameters of the nozzle

Equivalent diameter (mm)	0.28
Flow rate (kg/h)	5
Injection pressure (bar)	3.76
Reynolds number	6305
Ohnesorge number	0.00691

1200 consecutive images for a single location in the spray, with an exposure time of approximately 0.16 μs, taking approximately 14.3 ms to complete. For back illumination, a Cree LED XLamp XT-E Royal Blue was synchronized with the frame capturing rate of the camera sensor. The light from the LED was passed through a collimating lens before illuminating the spray. It is assumed that the liquid sheet and spray structures remain within the depth of field of the optical setup.

Mechanisms leading to breakup

During this study, we reproduced some results that were reported in the earlier studies. In [13, 14], it was observed that disintegration in liquid sheets is caused by three mechanisms, namely rim formation, waves and perforations.

At low relative velocities (Re<3000), the surface tension of the liquid creates thick rims along the periphery of the sheet. These rims flow downward and undergo impingement to form another sheet along the orthogonal plane of the rims. This process repeats until the momentum of the liquid within the rim is reduced to a point where a cylindrical liquid column is formed, which then breaks up due to Rayleigh–Plateau instability. Figure 3 illustrates liquid breakup through rim formation mechanism. As Reynolds number is increased (3000<Re<4000), perforations appear within the sheet that are enclosed by the rims produced by the same liquid that was initially inside. These holes grow, causing the rims of adjacent holes to coalesce, and form ligaments and droplets. These ligaments eventually lead to polydisperse droplets. The dynamics of perforations is presented in Figure 4.

At high Reynolds number (Re>4000), the spray breaks up due to vigorous waves (see Figure 5). The waves are named after Squire who first analysed stability in liquid sheets [15]. The wave disintegration is caused due to aerodynamic interaction between the sheet and surrounding air giving rise to Kelvin-Helmholtz type of instability.

Along the periphery of the liquid sheet, the stripping of ligaments and rim tear is caused due to Rayleigh–Taylor instability. As the ligament detaches, a trough is formed which deepens and aids in the breakup of the sheet. Figure 6 shows the formation of ligaments accompanied by satellite droplets.

Results and discussion

An image processing algorithm was developed to determine particle size and velocity distributions at all locations. Various image processing criteria were adopted to identify the structures and to analyse breakup. The methodology is described below.

It is assumed that the breakup is symmetric along the spray axis, and as the spray is quasi-steady, it was decided to capture only one side of the spray. A flat field correction was performed on grayscale images from the camera by dividing them by the white background image. This was followed by identifying perforations in images. To do so, connected component analysis of blobs was performed during which outliers such as intensity were defined to finally create a mask for the perforations. In a separate step, the images were binarised using Otsu's method to identify droplets.

It must be noted that due to the small field of view, multiple regions of the spray were captured along the horizontal and vertical direction synchronously, which were then stitched together to create a combined image (see Figure 7 (left)). Each individual image in the combined image is called image cell. The combined binary image was then taken through a chain of logical operations to identify perforations, liquid sheet and droplets as can be seen in Figure 8. This was followed by connected component analysis of structures during which location, size and shape of the structures are identified. The above process was applied across all 1200 consecutive time frames, which rendered more than 3

million structures.

The metrics potentially useful in ascertaining transition from liquid sheet to droplets are liquid fraction and entropy. The binarised image depicted in Figure 8 was averaged across 1200 consecutive images to represent overall liquid fraction in different regions of the spray. Figure 9(a) shows the liquid fraction for a quasi-steady flow at 5 kg/h. The normalised entropy of the spray is based on the formula [16]

$$E = -\frac{p_1 \ln p_1 + p_2 \ln p_2 + p_3 \ln p_3}{\ln 3} \tag{1}$$

where p_s is associated with the probability of states 1,2 and 3, calculated across 1200 consecutive images. Here 1, 2 and 3 refers to liquid sheet, droplets and air. p_s is calculated from the frequency of states at each pixel location. Figure 9(b) presents the normalised entropy for a steady flow rate of 5 kg/h. As for the case when only two states are present ($p_1 = 0$), the maximum value of $p_{2/3}$ is 0.5, hence the entropy cannot be greater than 0.631 [16]. When obtaining particle distributions, particles beyond 14 mm radius from the orifice were considered based on Figure 9.

The particles were mapped onto a 40×22 polar grid containing 840 grid elements. To avoid error due to stitches, the initial position $O_{x,y}$ of nozzle orifice in the reference imaging plane was offset along horizontal and vertical direction at the beginning of image acquisition using a micrometer adjustment. Four batches of data were acquired using this approach, each with a different offset, as shown in Figure 7(right). Particle statistics were calculated for each batch. However, gridding in a combined image created a bias toward smaller particles near the borders of image cells. To prevent this bias from affecting the statistics of the polar grid, the nearest centre approach was adopted. In the nearest centre approach, particles for a given grid element are selected from the batch whose image cell center was closest to the grid element center. In Figure 10, the color of a grid element indicates the batch selected to acquire statistics within that element based on the nearest center approach.

A grid resolution of 40×22 was sufficient to obtain more than 5000 particles per grid element in the denser regions, as shown in Figure 11(a). Properties such as Sauter mean diameter, number density, and polydispersity were evaluated and analyzed within each grid element, as required for the gFLA. To identify clustering of structures, we calculated the total number density, which represents the number of structures per unit area (in mm^2). These values were averaged across 1200 frames. It can be observed in Figure 11(b), that the total number density is lower in the transition region and along the periphery, which is due to formation of ligaments and rim tear respectively. Also the number density increases away from the orifice due to constant splitting of liquid bulk.

In the analysis of particle size distribution, the Sauter mean diameter is used to represent the overall size of particles within each grid element. The Sauter mean diameter (SMD or D_{32}), also known as the volume-surface mean diameter, is a statistical measure used to compute the average particle size in sprays. It is calculated using the following formula:

$$D_{32} = \frac{\sum_{i=1}^{n} n_i d_i^3}{\sum_{i=1}^{n} n_i d_i^2}, \tag{2}$$

where n_i is the number of particles in each size class i. In Figure 11(c), it can be observed that D_{32} is higher in the breakup region and along the periphery of the spray. To relate D_{32} with polydispersity of particles, Figure 11(d) illustrates standard deviation of particle sizes from their mean diameter, which indicates the level of polydispersity in the particle size distribution. It is seen that D_{32} correlates with polydispersity of particles, which is due to the formation of satellite droplets as ligaments strip from the rim.

For the gFLA, it is important to note that each grid element in Figure 11 corresponds to a particle distribution function. To illustrate this, we plot the probability density of particle sizes at 29.6 mm from the orifice and 2° from the longitudinal axis. The particle distribution function is found to be closer to log-normal as can be observed in Figure 12. The mean and variance of the log-normal function are tabulated for all grid elements such that they can be now be used in gFLA.

For velocity measurements, Particle Image Velocimetry (PIV) was considered to trace the most probable displacement of particles in the spray. An interrogation window size of 128 with 50% overlap was

selected and a single pass with repeated correlation was used [17]. As in the particle size statistics, combined images were considered in this study as well. The time resolved displacements were obtained for 1200 image pairs. The velocities are mapped on a square grid, with an interrogation window of 64×64 pixels. There was a cross over of interrogation windows along the stitches. To prevent this from affecting the velocity statistics of the grid, the nearest centre approach was adopted here as well. In Figure 13, the color of a grid element indicates the batch selected to acquire statistics within that element based on the nearest center approach. The displacements are multiplied by a calibration factor 0.3907 to convert from pix/frame to m/s. Figure 14 shows the mean velocities in the atomised and fluctuations in the velocities averaged across 1200 image pairs. For uniformity, the velocity statistics can be rearranged and mapped onto a similar polar grid 40×22, as presented in Figure 15. To support gFLA, the mean and variance of the log-normal velocity distribution function have been tabulated for all grid elements.

Conclusions

A new methodology has been developed to obtain local particle size and velocity distributions in sprays. The methodology uses four batches of consecutive stitched images to acquire statistics using the nearest centre approach. Several spray characteristics, including number density, Sauter mean diameter, polydispersity, velocity, and velocity fluctuations, were obtained for a flat fan spray.

Finally, the particle distributions have been tabulated at all locations to support gFLA. The results demonstrate the effectiveness of the methodology in accurately characterising spray behaviour, and it is believed that this approach will be a valuable tool for future research in this field.

Acknowledgements

References

[1] Sergei Sazhin. *Droplets and Sprays*. Vol. 9781447163. London: Springer, 2014. ISBN: 9781447163862. DOI: https://doi.org/10.1007/978-1-4471-6386-2.

[2] D.P Healy and J.B Young. "Full Lagrangian methods for calculating particle concentration fields in dilute gas-particle flows". In: *Proceedings of the Royal Society A: Mathematical, Physical and Engineering Sciences* 461.2059 (2005), pp. 2197–2225. DOI: 10.1098/rspa.2004.1413. eprint: https://royalsocietypublishing.org/doi/pdf/10.1098/rspa.2004.1413.

[3] Y. Li and O. Rybdylova. "Application of the generalised fully Lagrangian approach to simulating polydisperse gas-droplet flows". In: *International Journal of Multiphase Flow* 142 (2021), p. 103716. ISSN: 0301-9322. DOI: https://doi.org/10.1016/j.ijmultiphaseflow.2021.103716.

[4] Steven Begg et al. "Vortex ring-like structures in gasoline engines". English. In: *International Journal of Engine Research* 622 (2009), pp. 233–258. ISSN: 1468-0874.

[5] A. N. Osiptsov. "Lagrangian Modelling of Dust Admixture in Gas Flows". In: *Astrophysics and Space Science* 274.1 (Oct. 2000), p. 377. ISSN: 1572-946X. DOI: 10.1023/A:1026557603451.

[6] T. Gilet and L. Bourouiba. "Fluid fragmentation shapes rain-induced foliar disease transmission". In: *Journal of The Royal Society Interface* 12.104 (2015), p. 20141092. DOI: https://doi.org/10.1098/rsif.2014.1092.

[7] A.L. Yarin. "Drop impact dynamics: splashing, spreading, receding, bouncing..." In: *Annual Review of Fluid Mechanics* 38.1 (2006), pp. 159–192. DOI: 10.1146/annurev.fluid.38.050304.092144. eprint: https://doi.org/10.1146/annurev.fluid.38.050304.092144.

[8] Stefan Kooij et al. "What determines the drop size in sprays?" In: *Phys. Rev. X* 8 (3 July 2018), p. 031019. DOI: 10.1103/PhysRevX.8.031019.

[9] B. Abramzon and W. A. Sirignano. "Droplet vaporization model for spray combustion calculations". In: *International Journal of Heat and Mass Transfer* 32.9 (1989), pp. 1605–1618. ISSN: 0017-9310. DOI: `https://doi.org/10.1016/0017-9310(89)90043-4`.

[10] J. Anez et al. "Eulerian–Lagrangian spray atomization model coupled with interface capturing method for diesel injectors". In: *International Journal of Multiphase Flow* 113 (2019), pp. 325–342. ISSN: 0301-9322. DOI: `https://doi.org/10.1016/j.ijmultiphaseflow.2018.10.009`.

[11] Oyuna D. Rybdylova, Timur S. Zaripov, and Yuan Li. "Two-way coupling of the fully Lagrangian Approach with OpenFOAM for spray modelling". In: 2019.

[12] William D. Bachalo. "Spray Diagnostics for the Twenty-first Century". In: *Atomization and Sprays* 10.3-5 (2000), pp. 439–474. ISSN: 1044-5110.

[13] N. Dombrowski and R. P. Fraser. "A Photographic Investigation into the Disintegration of Liquid Sheets". In: *Philosophical Transactions of the Royal Society of London. Series A, Mathematical and Physical Sciences* 247.924 (1954), pp. 101–130. ISSN: 00804614.

[14] William A. Sirignano. *Fluid Dynamics and Transport of Droplets and Sprays*. Cambridge: Cambridge University Press, 2010. ISBN: 9780521884891. DOI: `https://doi.org/10.1017/cbo9780511806728`.

[15] H B Squire. "Investigation of the instability of a moving liquid film". In: *British Journal of Applied Physics* 4.6 (June 1953), pp. 167–169. DOI: `10.1088/0508-3443/4/6/302`.

[16] J.B. Blaisot and J Yon. "Entropy based image analysis for the near field of direct injection Diesel jet". In: *ILASS*. Nottingham, UK, 2004.

[17] William Thielicke and René Sonntag. "Particle Image Velocimetry for MATLAB: Accuracy and enhanced algorithms in PIVlab". In: *Journal of Open Research Software* 9 (2021). DOI: `10.5334/jors.334`.
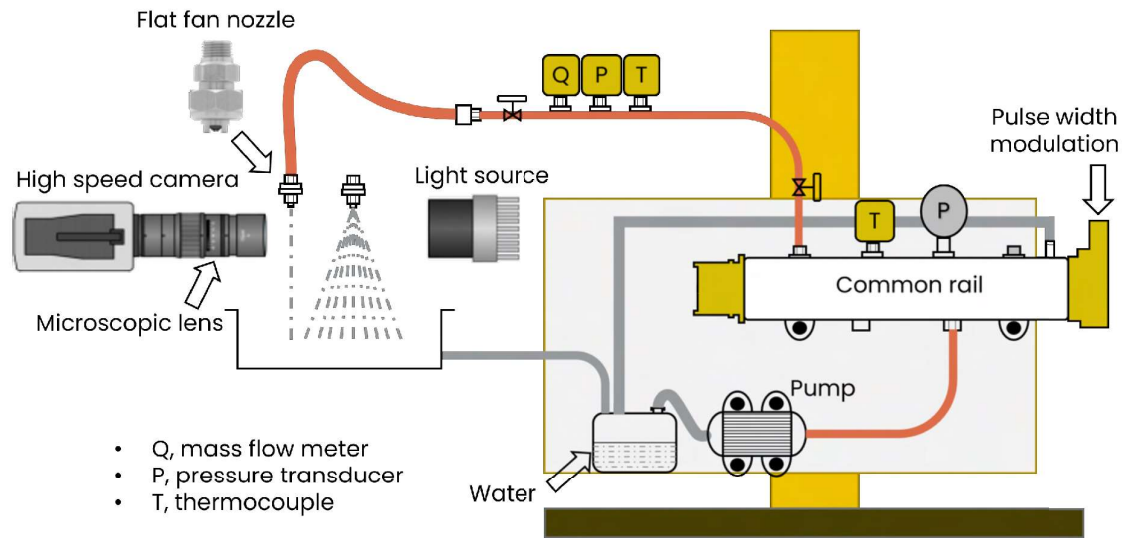
Figure 1. Schematic of a steady flow spray rig.

- Q, mass flow meter
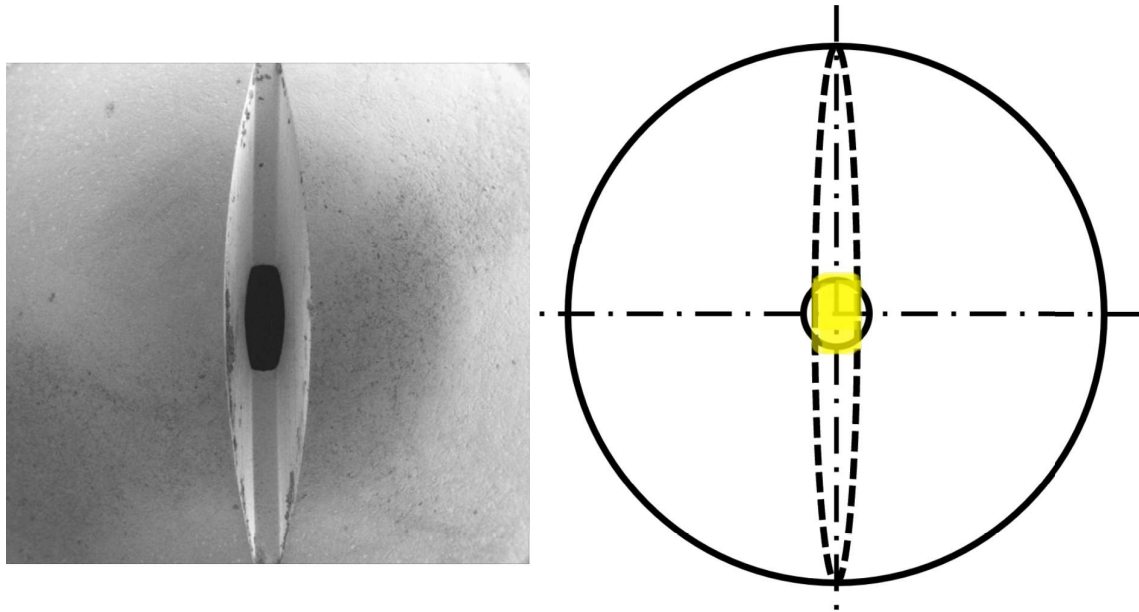- P, pressure transducer
- T, thermocouple

Figure 2. Microscopic view of a flat fan nozzle featuring elliptical orifice at the intersection of a circular hole and V notch.

Figure 3. Rim formation mechanism: (a) front view - primary Sheet, (b) side view - secondary sheet, and (c) breakup in the downstream region.
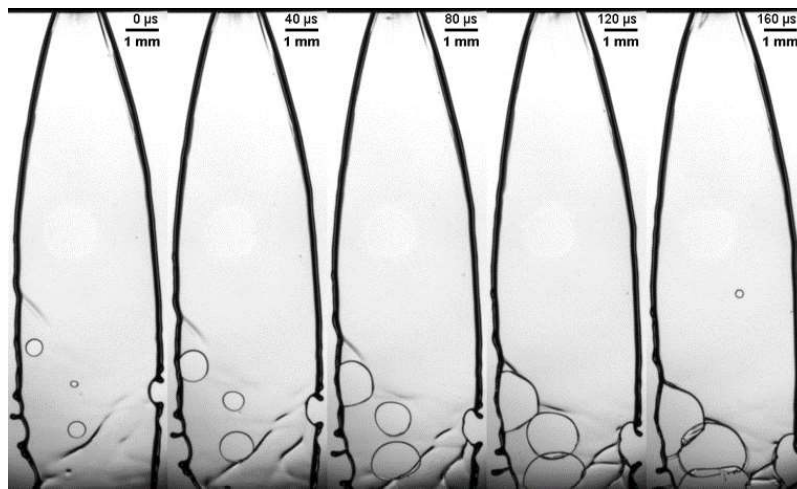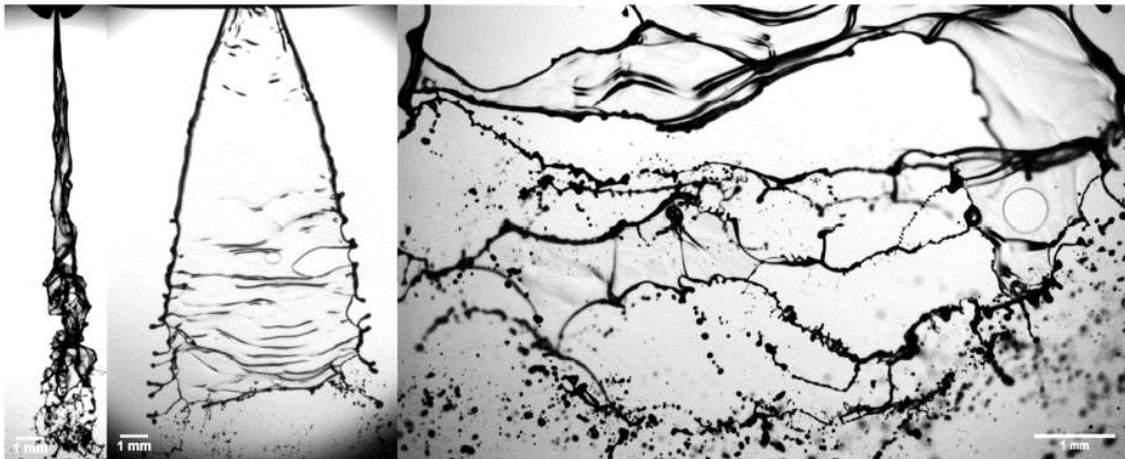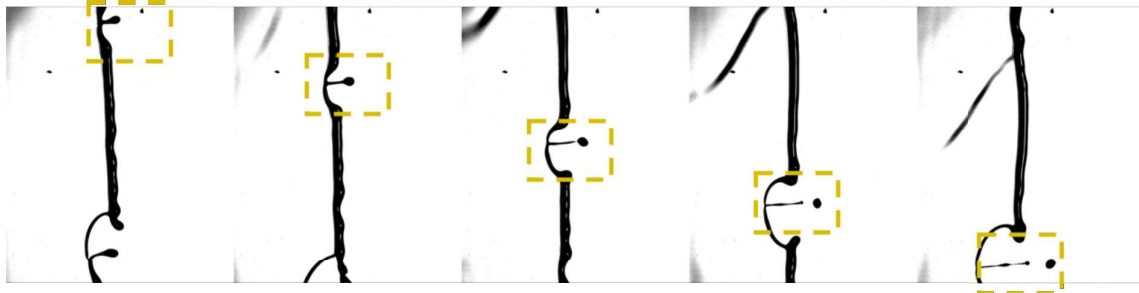

Figure 4. Dynamics of perforations in the liquid sheet.

Figure 5. Breakup of spray due to wave formation and perforations at high Reynolds number. In this regime, Squire waves form due to aerodynamic interaction between the sheet and surrounding air leading to Kelvin-Helmholtz instability.

Figure 6. Stripping of ligaments along the periphery due to Rayleigh–Taylor instability. Here the time between consecutive frames is 40 μs. As the ligament detaches from the rim, it deepens the trough which aids breakup of liquid sheet.
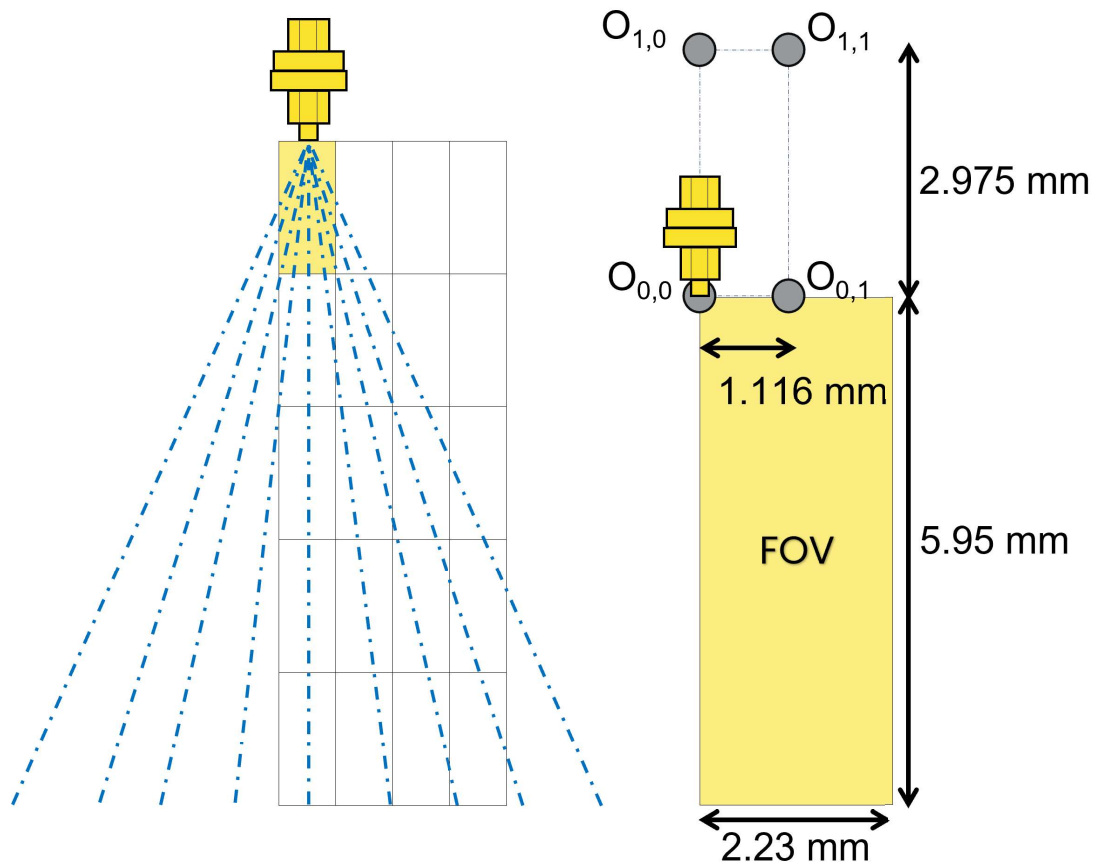
Figure 7. Position $O_{x,y}$ of the nozzle orifice in the reference imaging plane at the beginning of image acquisition. The nozzle is offset along horizontal and vertical direction using micrometer adjustment.
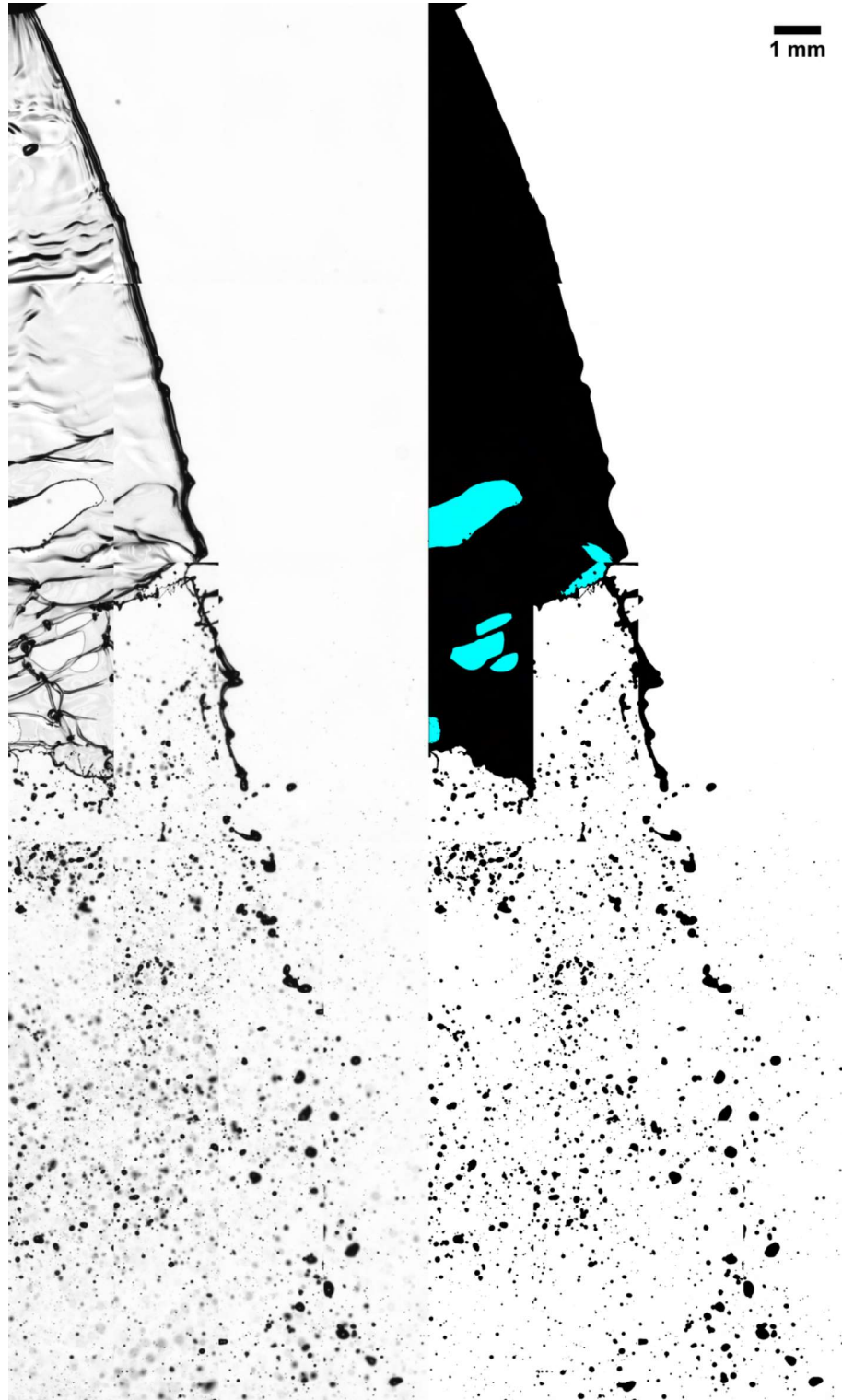
Figure 8. Stitched image of the spray identifying liquid sheet, perforations and droplets using developed image processing algorithm. The resolution of the image is 4.6 μm/pixel. The perforations are colored in blue while black represents continuous liquid sheet and dispersed droplets.
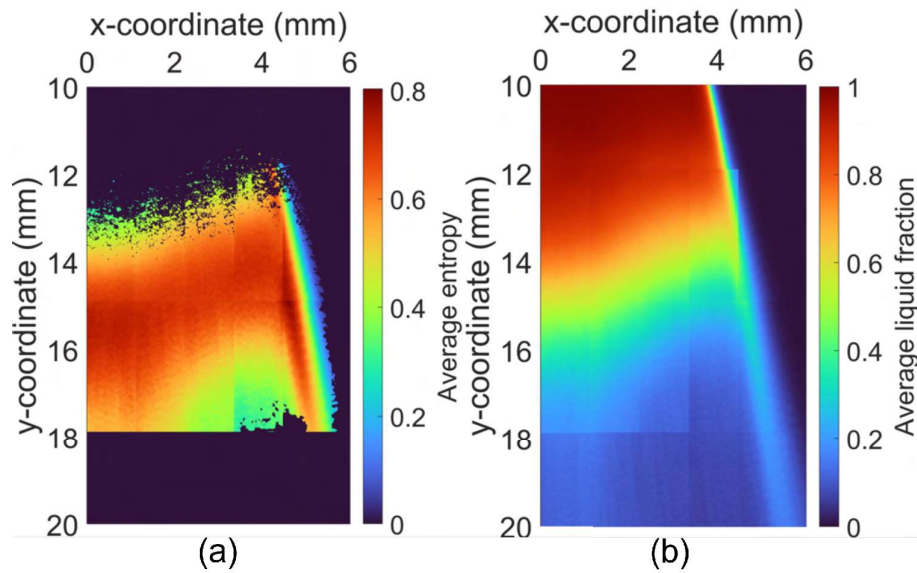
Figure 9. (a) Liquid fraction of the spray, where the regions with values closer to 1 signify continuous liquid sheet while the values closer to 0 indicate dispersed droplet phase, and (b) Entropy in the spray for states; liquid sheet, air and droplets.
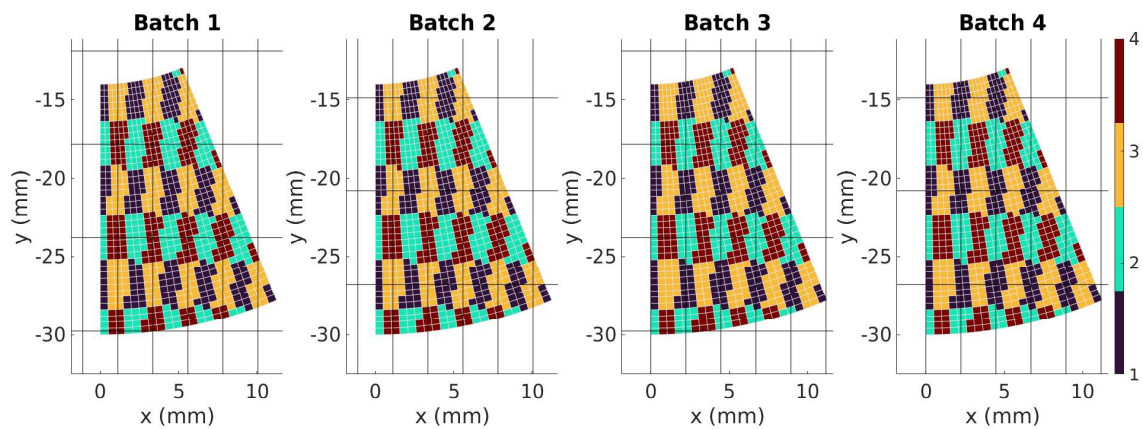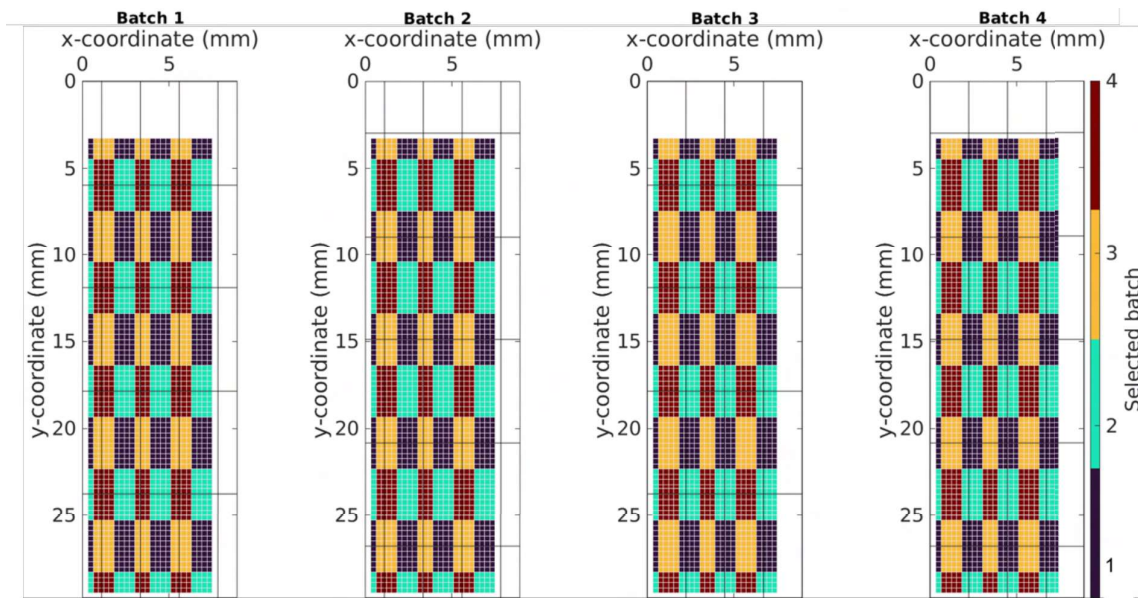

Figure 10. Division of spray into polar grid elements. The color of a grid element indicates the batch selected to acquire statistics within that element based on the nearest center approach.
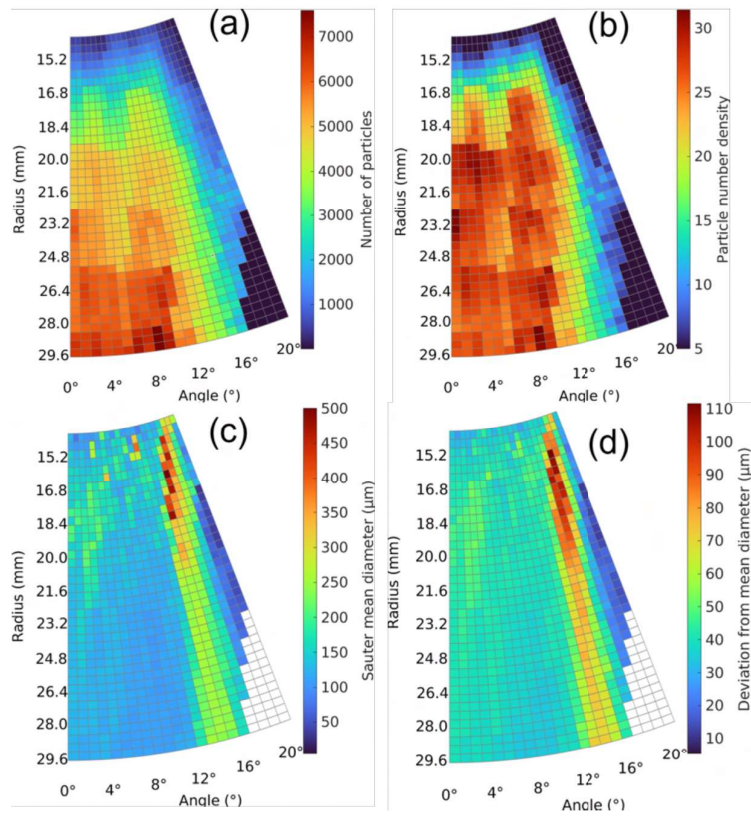
Figure 11. For mesh size 40×22, the size of a grid element is 0.4 mm×1°.Here, (a) number of particles, (b) number density of particles, (c) Sauter mean diameter, and (d) standard deviation from the mean diameter, which reflects polydispersity.
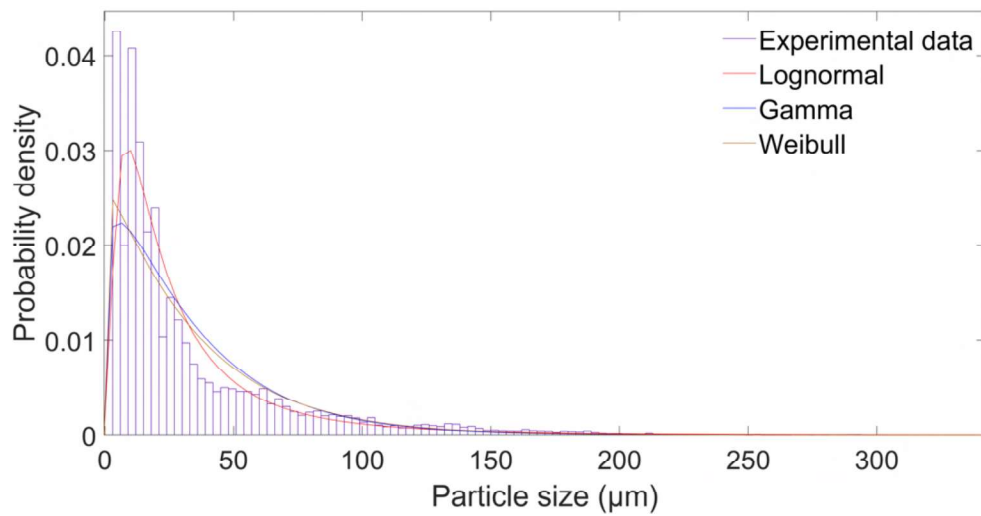

Figure 12. Probability distributions of droplet sizes (μm) at 29.6 mm from orifice and 2° from the longitudinal axis.

Figure 13. Division of a spray domain into 64×64 interrogation windows before performing cross correlation to obtain the most probable displacement of droplets between stitched image pairs. The color of a grid element indicates the batch selected to acquire velocity vectors within that window based on the nearest center approach.
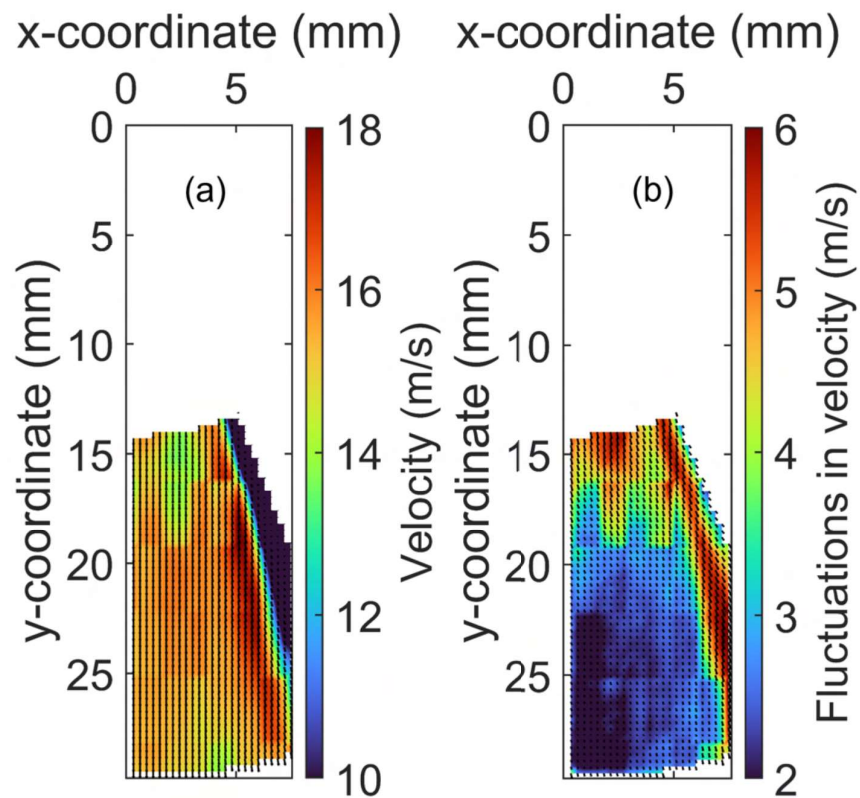
Figure 14. (a) Mean velocities in the atomised zone, and (b) standard deviation from mean velocity, which corresponds to velocity fluctuations.
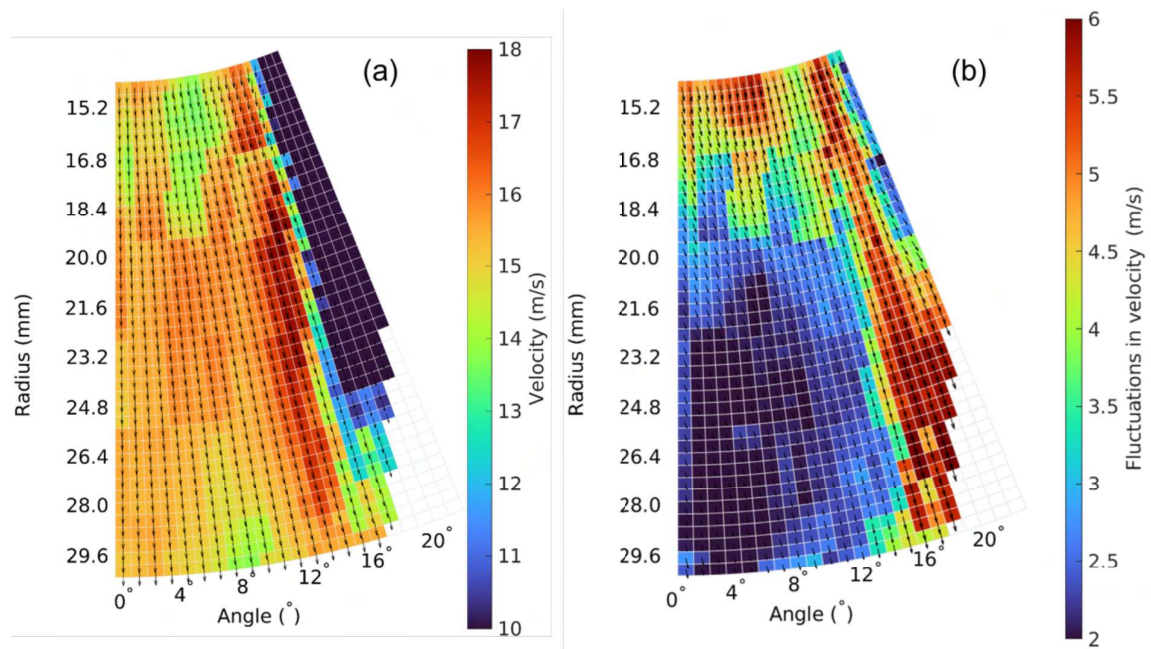
Figure 15. Apply transformation to polar coordinate system for (a) mean velocities in the atomised zone, and (b) velocity fluctuations.